

Fiber tract orientation dependent white matter signal in functional MRI

Jonathan Doucette^{a,b,*}, Luxi Wei^{a,c}, Enedino Hernández-Torres^{a,d}, Christian Kames^{a,b}, Nils Daniel Forkert^e, Rasmus Aamand^f, Torben E. Lund^f, Brian Hansen^f, and Alexander Rauscher^{a,b,d}

^aUBC MRI Research Centre, University of British Columbia, 2221 Wesbrook Mall, Vancouver, BC, Canada.

^bDepartment of Physics and Astronomy, University of British Columbia, 6224 Agricultural Road, Hennings Building, Room 325, Vancouver, BC, Canada.

^cDepartment of Medical Biophysics, University of Toronto, Toronto, ON, Canada

^dDepartment of Pediatrics, University of British Columbia Faculty of Medicine, Rm 2D19, 4480 Oak Street, BC Children's Hospital, Vancouver, BC, Canada.

^eDepartment of Radiology and Hotchkiss Brain Institute, University of Calgary, Calgary, AB, Canada.

^fCenter of Functionally Integrative Neuroscience (CFIN) and MINDLab, Department of Clinical Medicine, Aarhus University Hospital, Nørrebrogade 44, Building 10G, 5th floor, 8000 Aarhus C, Denmark.

March 27, 2018

Blood vessel related magnetic resonance imaging (MRI) contrast provides a window into the brain's metabolism and function. Here, we investigate the blood oxygenation level dependent (BOLD) MRI signal based on first principles derived from dynamic susceptibility contrast (DSC) MRI, diffusion tensor imaging (DTI), and theoretical considerations. We present a rapid numerical framework for the exploration of the isotropic and anisotropic components of the vascular tree and show that half of the white matter vascular volume is comprised of vessels running in parallel with white matter fibre tracts. The white matter blood volume corresponding to the best fit to the experimental data was 2.52%, which is very close to the PET gold standard of 2.6%. We show that the anisotropy of the brain's vascular architecture causes a strong tissue orientation dependence of the DSC MRI signal, with an apparent perfusion that is 20% larger in fibres perpendicular to the main magnetic field compared to parallel fibres. We then performed forward calculations of the BOLD signal for 3 and 7 Tesla and show that the gradient echo BOLD signal is twice as large in white matter tracts perpendicular to the main magnetic field compared to tracts parallel to the main magnetic field. For the spin echo BOLD signal, the orientation effect is about 20%. These findings have far reaching consequences for the interpretation of the existing literature on both functional and DSC MRI, as well as the conduction of future experiments using these techniques. The presented approach of fitting a vascular model to raw perfusion MRI data provides a new avenue for the measurement of global white matter blood volume.

The distribution of blood in the human brain is regulated via a specialized vascular network. Although the brain

comprises only 2% of the total body mass, it receives 15% of the cardiac output [1]. Cerebral blood flow (CBF), volume (CBV), and oxygenation are, thus, essential parameters of brain physiology and stable levels are required to maintain brain function. MRI is able to probe these parameters, usually via changes in the magnetic properties of the vascular system, to which the MRI signal is exquisitely sensitive. In DSC MRI, a paramagnetic contrast agent (CA) is administered intravenously during the repeated acquisition of a rapid imaging technique [2, 3]. BOLD fMRI uses changes in blood oxygenation for the detection of neural activity [4, 5]. The vast majority of fMRI studies focus on the brain's gray matter, but there are also reports on fMRI in white matter [6, 7, 8]. Very recently, a study in 176 subjects suggested functional networks that are related to specific white matter (WM) tracts [9]. The origin of the WM fMRI signal, however, is unclear. Potential sources are astrocytic activity [10, 11] and NO-producing neurons [12].

Both DSC MRI and BOLD fMRI data can be acquired with gradient echo or spin echo scans. In either case, the contrast mechanism is a change in coherence due to the field inhomogeneities around the blood vessels, which depend on CA concentration and blood oxygenation, and a change in intravascular relaxation times. With decreasing blood oxygenation or increasing CA concentration, the vessels become more paramagnetic and the field inhomogeneities become stronger [13, 4], which results in an accelerated loss of coherence. Analysis of fMRI and DSC scans usually assumes that the vascular architecture within the voxel is spatially isotropic, and therefore that the local orientation of the vasculature relative to the main magnetic field plays no role. However, there is compelling evidence that the vascular bed is not isotropic, particularly in white matter. Postmortem images show many vessels running in parallel with WM tracts [14, 15, 16]. Microscopic images of a rodent model of ischemia [17], and maps of perivascular spaces in humans [18] exhibit anisotropy of the vascular architecture. In venography based on susceptibility weighted imaging (SWI) [19, 20, 21], the anisotropy of the

*Corresponding author: jdoucette@phas.ubc.ca

vascular system can be readily appreciated *in vivo*. Finally, and especially important for functional MRI, the orientation of cortical tissue influences the strength of the BOLD signal [22].

It has been recently shown that the gradient echo perfusion signal and the maps of CBF and CBV derived therefrom show a strong dependence on the local orientation of WM fibre tracts [23]. Numerical simulations of static spin dephasing that best fit the measured data suggested that about half the blood volume is within larger anisotropic vessels [23].

Gradient echo scans are usually used for fMRI and DSC experiments, due to their high sensitivity to changes in blood oxygenation or CA concentration. However, spin echo scans are also sensitive to the presence of an intravascular CA or to changes in blood oxygenation because the spins lose coherence when they diffuse in the magnetic inhomogeneous environment created by the blood vessels [24]. Since smaller vessels produce stronger field gradients, the spin echo signal is more sensitive to small vessels than to large vessels. For this reason, spin echo fMRI is more specific to the location and spatial extent of neural activation [25, 26, 27]. If the vascular system is structurally isotropic, loss of coherence is orientation-independent. With anisotropic vascular architecture, on the other hand, the loss of coherence should depend on tissue orientation and give rise to orientation effects in MRI.

The anisotropy of the cerebral vasculature, in particular in WM, raises several questions: How strongly do the DSC and BOLD signals depend on the orientation of WM? How much blood resides in the isotropic and anisotropic compartment of the vascular network, and what is the role of vessel size? Finally, what are the implications of vascular anisotropy for BOLD fMRI?

In this work, we investigate the vascular architecture experimentally by combining spin echo DSC with diffusion tensor imaging for the analysis of WM fibre orientation. We then fit a model of the spin echo signal for fibre orientations between 0° and 90° from which we extract isotropic and anisotropic components of the vascular tree. These calculations require the solution of the Bloch-Torrey equation, which describes the spin echo signal in a magnetically inhomogeneous environment. Since we fit vascular parameters to the orientation dependent DSC signal, thousands of solutions of the Bloch-Torrey equation need to be computed on a large anisotropic 3D grid. To do so in a computationally feasible manner, we develop a framework that is based on the equivalence of the Bloch-Torrey equation to the single-particle time dependent Schrödinger equation. The vascular architecture that best fits the observed DSC signal is then taken as the input for a forward calculation of the BOLD signal at a range of echo times for both gradient echo and spin echo fMRI at 3 and 7 Tesla.

Materials and Methods

Theoretical Considerations

We first develop a numerical framework for the investigation of the effect of field inhomogeneities on the DSC signal. The simulation contains a small number of free parameters, which will be determined by fitting the simulated DSC signal data to the corresponding experimental data in a non-linear least squares fashion. These parameters will then be used for a forward calculation of the BOLD effect in WM.

The simulated DSC data is the change in transverse relaxation ΔR_2 that occurs due to the administration of the paramagnetic CA. This change in R_2 can be computed by simulating the magnetization within a single WM voxel until an echo time TE, both with and without CA. The resulting ΔR_2 is given by

$$\Delta R_2 = -\frac{1}{TE} \ln \left(\frac{S}{S_0} \right), \quad (1)$$

where S_0 is the signal before the arrival of the CA, and S is the signal at the time point corresponding to peak CA concentration [2, 3]. In order to investigate the effect of WM fibre tract orientation on the resulting ΔR_2 values, we define α to be the angle between the main magnetic field and the WM fibre and allow α to vary between 0° and 90° in the simulations. The two major components of the simulations are the generation of the geometry of the problem for a given set of simulation parameters, and the subsequent propagation of the magnetization through time.

The simulation takes place inside a single voxel of dimensions $3 \times 3 \times 3 \text{ mm}^3$, corresponding to the scan used to acquire the data. Inside this voxel, we place an isotropic vascular bed consisting of small blood vessels ($\sim 10 \mu\text{m}$), as well as anisotropic vasculature consisting of a variable number L of large blood vessels ($\sim 100 \mu\text{m}$) running in parallel with the z -axis. An example of this geometry with $L = 5$ anisotropic vessels is shown in Figure 1. The orientation of the WM fibres is assumed parallel to the anisotropic blood vessels [14, 15, 16, 17, 18, 19], and therefore the WM fibre is oriented in the z -direction as well. The total amount of vasculature contained in the voxel is determined by the blood volume fraction (BVF), a free parameter. The isotropic vasculature is simulated as cylinders with uniformly random orientation and position within the voxel, with radii of $7.0 \mu\text{m}$ [28]. The total number of isotropic vessels is determined by a second free parameter, the isotropic relative blood volume fraction (iRBVF). The anisotropic vasculature is simulated as uniformly spaced cylinders with axes parallel to the z -direction. The radii of the anisotropic vessels are determined by the anisotropic relative blood volume fraction (aRBVF), a constrained parameter given by $\text{aRBVF} = 1 - \text{iRBVF}$.

The voxel may now be thought of as being separated into vasculature and the surrounding tissue. In these regions, we prescribe different values for the relaxation rate R_2 and for the magnetic susceptibility χ . Additionally, the value of both R_2 and χ within the blood depends on the peak CA concentration (CA_{PEAK}), the third free parameter of the simulation. The dependence of R_2 and χ on CA_{PEAK} is detailed in our previous study; see equation 4 in [23]. Since χ is non-constant within the voxel, local magnetic field inhomogeneities are induced according to equation 2

$$\frac{\delta B(\mathbf{r})}{B_0} = G_\alpha(\mathbf{r}) * \delta\chi(\mathbf{r}), \quad (2)$$

where G_α is the unit dipole kernel defined as

$$G_\alpha(\mathbf{r}) = \frac{1}{4\pi} \frac{3 \cos^2(\theta) - 1}{r^3}. \quad (3)$$

This is the forward field calculation for the magnetic field by convolution of the spatial magnetic susceptibility distribution with a unit dipole [29]. The spherical radial distance and polar angle (r, θ) in equation 3 are relative to the main magnetic field direction. In our simulations, it is convenient to work in coordinates where the WM fibre is in the z -direction, hence the subscript α on the dipole kernel. The resulting local resonance frequency shift seen by the diffusing protons is given by

$$\delta\omega(\mathbf{r}) = \gamma \cdot \delta B(\mathbf{r}). \quad (4)$$

In the experimental data, α was computed by taking the angle between the main magnetic field direction and the principal diffusion direction as measured with DTI. Each WM voxel was then sorted into bins according to their α -value. The bin widths were taken to be 5° , resulting in 18 bins corresponding to angles from 2.5° to 87.5° in 5° increments. In the numerical simulations, α varies over these 18 angles in order to match the experimental data. Cross sections of $\delta\omega$ in the xy -plane for three different angles α are shown in Figure 1.

Next, we consider the propagation of the magnetization through time, which is described by the Bloch-Torrey equation [30]

$$\frac{d\mathbf{M}}{dt} = \gamma \mathbf{M} \times \mathbf{B} - \left[\frac{M_x}{T_2}, \frac{M_y}{T_2}, \frac{M_z - M_0}{T_1} \right]^T + \nabla \cdot \mathbf{D} \nabla \mathbf{M}. \quad (5)$$

Accounting for diffusion in the presence of the α -dependent field inhomogeneities introduces α -dependent simulated ΔR_2 values.

Since $TE \approx T_2 \ll T_1$, we neglect T_1 effects. We assume isotropic diffusion by setting $\mathbf{D} = D\mathbf{I}$. Additionally, we denote

$$\mathcal{M} := M_x + iM_y \quad (6)$$

the complex transverse magnetization and

$$\Gamma(\mathbf{r}) := R_2(\mathbf{r}) + i\omega(\mathbf{r}) \quad (7)$$

the complex decay rate, where $\omega(\mathbf{r}) = \omega_0 + \delta\omega(\mathbf{r})$ with $\omega_0 = \gamma B_0$, and $R_2(\mathbf{r})$ is the piecewise constant R_2 value taking different values in tissue and in blood. The resulting Bloch-Torrey equation is

$$\frac{\partial}{\partial t} \mathcal{M}(\mathbf{r}, t) = D \nabla^2 \mathcal{M}(\mathbf{r}, t) - \Gamma(\mathbf{r}) \mathcal{M}(\mathbf{r}, t), \quad (8)$$

where ∇^2 is the 3D Laplacian operator. The Bloch-Torrey equation admits no closed form for general $\Gamma(\mathbf{r})$, and must be solved numerically.

At this point, we change coordinates such that the WM fibre is in z -direction and so \mathcal{M} represents the magnetization transverse to the magnetic field $\mathbf{B} = B_0[\sin \alpha, 0, \cos \alpha]^T$. This is purely a matter of convenience, as now instead of generating new vasculature networks for each desired WM fibre angle α , the WM fibres can remain fixed and only the frequency shifts $\delta\omega(\mathbf{r})$ must be recomputed.

The simulation contains four free parameters: the peak contrast agent concentration CA_{PEAK} , the total blood volume fraction BVF, the isotropic relative blood volume fraction iRBVF, and the total number of large anisotropic vessels L . The task is now to find parameters such that the solutions to equation 8 result in a ΔR_2 vs. α curve that is as close as possible to the experimental ΔR_2 vs. α data. The basic algorithm to do so is as follows: for a given number of anisotropic vessels L choose an initial set of parameters CA_{PEAK} , BVF, and iRBVF; for each angle α calculate the corresponding 3D map of resonance frequencies and initialize the magnetization with the constant value of $\mathcal{M}_0 = i = \sqrt{-1}$; propagate the magnetization by solving the Bloch-Torrey equation both with and without CA for each angle α to obtain a simulated ΔR_2 vs. α curve; compare the resulting curve with the observed ΔR_2 vs. α data set; choose new parameters based on an error minimization algorithm such as gradient descent; repeat until convergence of parameters. Approximately 25-30 iterations are needed for convergence for a typical set of parameters to a tolerance on the order of 0.1% with an appropriate initial guess. Due to the fact that the Bloch-Torrey equation must be solved both with and without CA for each of the 18 angles α , approximately 1,000 solutions to the Bloch-Torrey equation must be computed. For this reason, and because the anisotropic nature of the vascular tree requires a simulation in three dimensions, rapid computation is required.

Fast Solution of the Bloch-Torrey Equation

In order to solve equation 8 efficiently, we begin by considering techniques used to solve the *imaginary-time* Schrödinger equation [31], which is equivalent to the Bloch-Torrey equation 8 [32, 33]. In this analogy, $-D\nabla^2$ is the kinetic energy operator, and Γ is the *complex* potential energy.

This allows us to use *Diffusion Monte Carlo* (DMC) techniques for solving the Bloch-Torrey equation 8. DMC methods were originally developed to solve the imaginary-time Schrödinger equation by directly approximating the evolution operator $\exp(-\hat{H}t)$ which acts on an initial wavefunction $\Psi(\mathbf{r}, t = 0)$, where \hat{H} is the Hamiltonian of the system. In our case, $\hat{H} = -D\nabla^2 + \Gamma$ and $\Psi(\mathbf{r}, 0) = \mathcal{M}(\mathbf{r}, 0)$. We use a particular set of DMC methods known as *splitting methods*, wherein the evolution operator of the imaginary-time Schrödinger equation is approximated over sufficiently small time intervals Δt . We have the approximations [34, 35]

$$e^{-\hat{H}\Delta t} = e^{(D\nabla^2 - \Gamma)\Delta t} \quad (9)$$

$$= e^{D\nabla^2\Delta t} e^{-\Gamma\Delta t} + \mathcal{O}(\Delta t^2) \quad (10)$$

$$= e^{-\Gamma\Delta t/2} e^{D\nabla^2\Delta t} e^{-\Gamma\Delta t/2} + \mathcal{O}(\Delta t^3). \quad (11)$$

The error terms in equations 10 and 11 occur due to the fact that the operators $D\nabla^2$ and Γ do not commute. Otherwise, these approximations would both be exact. Although the Hamiltonian is not Hermitian, as is typically the case in quantum mechanics, hermiticity is not required for splitting methods.

Importantly, the action of the evolution operators $e^{D\nabla^2 t}$ and $e^{-\Gamma t}$ in approximations 10 and 11 are known [34]

$$e^{D\nabla^2 t} \mathcal{M}_0(\mathbf{r}) = \Phi(\mathbf{r}, t) * \mathcal{M}_0(\mathbf{r}) \quad (12)$$

$$e^{-\Gamma t} \mathcal{M}_0(\mathbf{r}) = e^{-\Gamma(\mathbf{r})t} \mathcal{M}_0(\mathbf{r}), \quad (13)$$

where $\Phi(\mathbf{r}, t)$ is the Gaussian kernel defined as

$$\Phi(\mathbf{r}, t) := \frac{1}{(4\pi Dt)^{3/2}} e^{-\mathbf{r}^2/4Dt} \quad (14)$$

and $*$ denotes the convolution over space. Note that, as opposed to equation 9, the evolution of the initial transverse magnetization \mathcal{M}_0 via equation 12 or 13 is extremely fast to compute. Equation 12 simply convolves the initial state with the Gaussian kernel (or equivalently, it applies uniform smoothing of width $\sigma = \sqrt{2Dt}$). This convolution can be computed efficiently using the Fast Fourier Transform (FFT), since the boundary conditions are taken to be periodic [36]. Equation 13 involves pointwise multiplication and exponentiation, and thus is even faster to compute.

The approximate solutions given by equations 10 and 11 can be thought of as follows: instead of allowing decay and diffusion to occur simultaneously using \hat{H} , the signal undergoes pure decay due to Γ and pure diffusion due to $D\nabla^2$ in an alternating fashion over small time steps of order Δt , repeating until the desired time t is reached.

We are now in a position to solve the Bloch-Torrey equation efficiently. We begin by discretizing the $3 \times 3 \times 3 \text{ mm}^3$ voxel into N^3 subvoxels. The subvoxels need to be small enough that diffusion effects can be captured during each time step, but large enough that solving the

system is still computationally feasible. The root mean square distance travelled by a freely diffusing particle in n -dimensions is [37]

$$d_{rms} = \sqrt{2nD\Delta t}. \quad (15)$$

If we choose $\Delta t = \text{TE}/30 = 2 \text{ ms}$ and the diffusion constant $D = 3.037 \mu\text{m}^2/\text{ms}$ [38], the mean free diffusion distance in $n = 3$ dimensions is $d = 6.04 \mu\text{m}$. Choosing $N = 512$ gives a subvoxel size of $5.86 \mu\text{m}$, capturing diffusion effects while being computationally feasible.

Algorithm 1 details how to compute the signal at time TE using the approximate evolution equation 10. To assess the accuracy of the approximate solution from Algorithm 1, we compute the solution of equation 8 directly. This can be achieved by first discretizing the Hamiltonian operator using the method of lines [39], wherein space is discretized into a set of gridpoints \mathbf{r}_i , the Laplacian ∇^2 is approximated using standard second-order centred finite differencing, and Γ is a diagonal matrix consisting of the values $\Gamma(\mathbf{r}_i)$. This process represents the Hamiltonian \hat{H} as a matrix \mathbf{H} , and the magnetization $\mathcal{M}(\mathbf{r}, t)$ as a vector $\mathbf{M}(t)$, where each element $\mathcal{M}_i(t)$ represents $\mathcal{M}(\mathbf{r}_i, t)$. The Hamiltonian matrix \mathbf{H} then acts on the transverse magnetization \mathbf{M} through matrix multiplication. The resulting discretized forms of equations 8 and 9 are

$$\frac{\partial}{\partial t} \mathbf{M}(t) = -\mathbf{H} \mathbf{M}(t) \quad (16)$$

$$\Rightarrow \mathbf{M}(t) = e^{-\mathbf{H}t} \mathbf{M}(0), \quad (17)$$

where the notation $e^{-\mathbf{H}t}$, in this context, represents the *matrix exponential* [40] of the matrix $-\mathbf{H}t$. In our case, although $\mathbf{H} \in \mathbb{C}^{N^3 \times N^3}$ where $N = 512$ is extremely large, we need only compute the matrix exponential vector product (also known as the *action* of the matrix exponential), and not $\exp(-\mathbf{H}t)$ itself, which is in general full despite \mathbf{H} being sparse [40]. Algorithms for computing the action of the matrix exponential are known [41, 42]. We use the algorithm described by Higham et al. in [43], as well as their MATLAB code *expmv*. A comparison of the signal resulting from Algorithm 1 versus equation 17 and *expmv* is shown in Figure 2, revealing that the difference between the approximate and exact solution is less than 0.2%. However, the exact solution with *expmv* is almost two orders of magnitude slower than approximations 10 or 11, making it unsuitable for parameter fitting.

We are now able compute a solution to the original problem of fitting the simulated ΔR_2 vs. α curve to the observed data on a PC with an Intel Core i7-3930K CPU and 32GB of memory running Gnu/Linux within less than a day rather than several weeks. An initial set of simulation parameters (BVF, iRBVF, CA_{PEAK} , and L) are chosen, and the Bloch-Torrey equation 8 is propagated numerically using Algorithm 1 until time $\text{TE} = 60 \text{ ms}$. ΔR_2 is subsequently calculated for each angle α using equation 1. For L ranging from 1 to 9

the corresponding optimal simulation parameters BVF, iRBVF, and CA_{PEAK} are determined through a gradient descent based non-linear ℓ^2 -norm minimization algorithm using MATLAB's *lsqcurvefit* [44].

Using the vascular architecture obtained from the DSC experiment, we then performed a forward calculation of the BOLD effect for gradient and spin echo fMRI of WM tracts at 3 and 7 T. We assumed a venous blood volume of two thirds of the total blood volume [45, 46], and a venous blood oxygenation of 0.61 at rest and 0.73 after activation [47]. The corresponding T_2 relaxation times are 33.3 ms and 49.7 ms at 3 T [47], and 14.1 ms and 21.9 ms at 7 T [48]. Arterial blood oxygenation was set to 0.98 [47]. The BOLD signal was calculated for echo times up to 120 ms and WM tract angles between 0° and 90° .

Experimental Procedures

Standard protocol approval, registrations and patient consents

This study was approved by the Clinical Research Ethics Board (Videnskabsetiske Komitéer for Region Midtjylland, M-2013-239-13, August 5th 2013) and is in accord with the Declaration of Helsinki. All subjects gave written informed consent.

Data acquisition

Data from 10 healthy subjects (3 female, age = 34 - 65 years, mean = 47.24 years) were acquired on a 3 T system (Skyra, Siemens, Erlangen, Germany). DSC was acquired with spin echo EPI (300 repetitions, TE = 60 ms, TR = 1530 ms, flip angle = 90° , voxel volume = $3 \times 3 \times 3 \text{ mm}^3$). 0.2 mmol/kg body weight of Gadovist (Bayer) was injected at a rate of 5 ml/s starting at scan 200, followed by a 30 ml saline flush. Fibre orientation was calculated from a diffusion tensor scan acquired for diffusion kurtosis imaging with a 1+3+9 scheme (b-values = 0/1000/2500 s/mm², voxel size = $2.29 \times 2.29 \times 2 \text{ mm}^3$, TE = 101 ms, TR = 12200 ms) [49].

Data processing

Fibre orientation maps were computed from the $b = 0$ and 2500 s/mm² data of the diffusion scan using the approach presented previously [23]. Motion correction, eddy current correction, brain extraction, and computation of the DTI data were performed using FSL [50]. The DSC data were motion corrected, brain extracted, and registered into DTI space via the fractional anisotropy maps using FSL.

Next, the DSC signal in each WM voxel was sorted into bins according to α , the local angle with respect to the main magnetic field B_0 , as determined through the

diffusion tensor scan [51]. The voxels of the DSC signal data were split into 18 bins centred around the angles ranging from 2.5° to 87.5° in 5° increments. Each bin was then averaged, resulting in a set of 18 signal vs. time curves parameterized by α . The last step was to calculate ΔR_2 for each curve according to equation 1.

For each voxel, the time point with the lowest T_2 signal was selected as the time point with peak CA concentration. The resulting set of data is a peak ΔR_2 vs. α curve with 18 data points, and it is this set of data that is compared with numerical simulations. In addition, CBF, CBV, and MTT were also calculated as function of fibre orientation, as described previously for gradient echo DSC [23, 51].

The perfusion parameters CBF, CBV, and MTT were estimated using a parametric approach informed by a physiological model of the microvasculature [52, 53]. In this approach, it is assumed that the intravascular contrast agent reaches the capillary bed at a particular blood concentration $C(t)$ modulated by the constant κ , which depends on hematocrit but is assumed constant here. The contrast agent concentration and CBF are then related via

$$\kappa C(t) = \text{CBF} \int_0^t C_\alpha(t - \tau) R(\tau) d\tau, \quad (18)$$

where $C_\alpha(t)$ denotes the arterial input function and $R(t)$ the residue function. The transport function $h(t)$, used to estimate the residue function, is parameterized as a gamma distribution

$$h(t; \alpha, \beta) = -\frac{dR}{dt} = \frac{1}{\beta^\alpha \Gamma(\alpha)} t^{\alpha-1} e^{-t/\beta}, \quad \alpha, \beta > 0. \quad (19)$$

In this approach, MTT equates to $\alpha\beta = \text{CBV}/\text{CBF}$, where CBF is the peak of the estimated residue function.

Results

The presence of CA in WM vasculature causes a change in ΔR_2 that depends on local WM fibre orientation measured with diffusion MRI (Figure 3). In WM perpendicular to the main magnetic field, ΔR_2 is 20% larger than in fibres parallel to the main magnetic field, as shown by the blue curve in Figure 3, which represents the average across data acquired in the 10 healthy volunteers. Moreover, the simulated ΔR_2 also depends considerably on the simulated vascular architecture. Since the loss of coherence is mediated by diffusion, not only does the total volume of the blood vessel compartments play a role, the vessel sizes do as well. The simulation with $L = 4$ anisotropic blood vessels with a radius of 96.9 μm is highlighted in red, as it provided the lowest average error compared to the observed data.

The simulated and measured curves represent a combination of an isotropic vascular component, which results in a

constant offset, and an anisotropic component, which results in the observed orientation dependence. Simulations of only an isotropic vascular bed exhibit no angle dependence, whereas the simulation of only the anisotropic vasculature exhibits no offset (not shown), which is in agreement with our earlier findings for gradient echo DSC [23].

The best fit resulted from $L = 4$ anisotropic vessels with a peak contrast agent concentration of $CA_{\text{PEAK}} = 6.39 \text{ mM}$ and a total blood volume fraction of $BVF = 2.52\%$, where $iRBVF = 46.8\%$ of the blood is contained in the isotropic vasculature and $aRBVF = 53.2\%$ of the blood is contained in the anisotropic vasculature. The radii of the anisotropic vessels range from $57.4 \mu\text{m}$ for 9 vessels to $217.6 \mu\text{m}$ for 1 vessel. The best fit corresponds to a vessel radius of $96.9 \mu\text{m}$, with next best fits occurring for $L = 3$ and $L = 5$ vessels with radii of $110.3 \mu\text{m}$ and $84.4 \mu\text{m}$, respectively.

The orientation dependence in ΔR_2 translates to corresponding orientation dependencies in the measured CBF, CBV, and MTT, as shown in Figure 4. Both CBV and CBF are about 20% larger in WM perpendicular to the main magnetic field compared to WM parallel to the main magnetic field, whereas the temporal parameter MTT shows only a small angle dependence.

Finally, the vascular architecture derived from the DSC experiment was fed into a forward calculation of the BOLD effect. Figure 5 shows the relative BOLD signal as a function of orientation and echo time at 3 and 7 T. In particular for echo times typically used in fMRI, the gradient echo BOLD signal exhibits a strong orientation dependence at both 3 and 7 T, with the signal almost twice as large for WM perpendicular to \mathbf{B}_0 compared to WM parallel to \mathbf{B}_0 . For small angles, the signal behaviour is dominated by the two discrete resonance frequencies inside and outside the vessel, resulting in a more complex signal behaviour over time, similar to previous observations for the signal decay around single vessels [54]. At larger angles, the extravascular field inhomogeneities contributions increase, resulting in a continuum of resonance frequencies. For angles close to the magic angle of 54.7° , the intravascular field and the field far from the vessel are very similar and the signal behaviour is dominated by the extravascular field. Considerable angle dependence is present at echo times of 20 ms and above. For the spin echo signal at 3 T, the diffusion around the larger vessels has no relevant influence up to echo times (i.e. diffusion times) of about 40 ms and the BOLD signal is dominated by the isotropic vascular bed with small vessel diameters. At 7 T, where the field gradients around the vessels are stronger, relevant orientation effects start to appear at 30 ms. However, even for longer TE, the orientation effect of the spin echo signal does not exceed 20% at either field strength. For very long echo times beyond 100 ms, the orientation dependence is attenuated by T_2 and T_2^* relaxation.

At both field strengths, the spin echo BOLD signal

peaks later than the gradient echo BOLD signal, which is expected, since it requires diffusion in addition to the static field inhomogeneities. Furthermore, the unscaled spin echo BOLD signal is almost the same at 3 and 7 T, which is due to the reduced T_2 -times of tissue at 7 T, which attenuates the field strength related gain in spin echo BOLD contrast. If the tissue T_2 -times at 7 T were the same as at 3 T, the scaled BOLD contrast at 7 T would be 50% higher (not shown).

Discussion

Solution of the Bloch-Torrey Equation

We have shown that spin echo DSC measurements depend on WM fibre orientation. We presented a rapid approach for parameter fitting that allows us to derive vascular parameters from the DSC signal. For solving the Bloch-Torrey equation [8], we introduced an algorithm which is based on techniques originally developed for quantum mechanics. This algorithm approximates the Green's Function of the Bloch-Torrey equation - which cannot be expressed analytically - over small time steps Δt . These intermediate solutions are iteratively updated during each time step until the desired time TE is reached. This method results in solutions that are within a fraction of a percent of the solution computed directly through matrix exponential methods, as illustrated by Figure 2. Importantly, the solution found by this algorithm is typically at least an order of magnitude faster to compute for typical simulation parameters than traditional approaches. This is a large advantage over the direct method, as this approach allows us to rapidly investigate varying complex 3D geometries and move quickly through the parameter space. In particular, the minimization to produce Figure 2 could be performed on a personal computer within less than a day, rather than weeks.

While the identification between the Bloch-Torrey equation and the imaginary-time Schrödinger equation has been known, methods used to solve the Bloch-Torrey equation that take advantage of quantum-inspired techniques typically use eigenfunction expansion based approaches [55], which are appropriate for quantum mechanical systems. However, these techniques are not useful for large 3D simulations of magnetized spins. As the eigenfunction decomposition is expensive, speed is largely completely sacrificed to begin with. Moreover, the goal of solving the Schrödinger equation in physical systems generally revolves around computing the ground state and the ground state energy, and possibly a small number of excited states above that. In our case, however, we are interested in propagating an initial state through time. Such an approach would require a suitably large eigenbasis in order to represent the magnetization accurately, and this

would be prohibitively expensive both to store in memory and to compute.

For these reasons, the Bloch-Torrey equation has most commonly been solved using finite element based [36] or finite difference based techniques. Such approaches are feasible if only one solution is computed, for example the BOLD effect for a particular vascular geometry, especially when said geometry is given in terms of a realistic vasculature mesh. However, as with matrix exponential based methods, these approaches are too slow and expensive for our problem of iterating through parameter space with the goal of *determining* the vascular geometry associated with an experimental DSC signal; we need to be able to quickly generate vascular geometries programmatically based on parameters such as BVF and iRBVF.

Using the method of lines to generate geometries, along with Algorithm 1, provides a balance between accuracy and speed in solving the Bloch-Torrey equation. Additionally, due to the separation of the diffusion and static decay processes, modifying the model is straightforward. For example, the decay process could be modified to allow for a fraction of vessels to be (partly) embedded in cerebrospinal fluid. Or, the isotropic diffusion step could be replaced with an anisotropic diffusion step, modifying the diffusion evolution operator (equation 12) with the rest of the algorithm remaining unchanged.

Perfusion Experiment

We found that the apparent perfusion parameters measured with spin echo DSC imaging depend on the WM fibre orientation, with ΔR_2 , CBF, and CBV increasing for increasing angles between WM and the main magnetic field, while the effect was rather small for MTT. An explanation for this phenomenon consistent with current scientific knowledge is that a proportion of the vascular network in WM runs in parallel with the fibre tracts. Solving the Bloch-Torrey equation for a range of vascular architectures and CA concentrations and fitting the results to the DSC signal reveals that about half of WM blood volume is in vessels that run in parallel with the fibre tracts, giving rise to orientation dependent field inhomogeneities.

The finding that 53% of the blood resides within anisotropic vasculature and 47% in the isotropic component is in good agreement with our earlier gradient echo experiment [23] in a different cohort. Simulations based on a larger isotropic vessel radius of $13.7 \mu\text{m}$ [56] result in a total blood volume fraction of 3.5%, an anisotropic blood volume fraction of about 34%, and an optimal $L = 5$ large vessels with radii of $81.5 \mu\text{m}$. An explanation for the larger total blood volume is that the spin echo experiment is less sensitive to larger vessels [24]. Larger vessels create field inhomogeneities with lower spatial frequencies, causing diffusion to happen within a locally more homogeneous

environment. In other words, the spin echo experiment is sensitive to the size of the vessels, in addition to blood volume. Nevertheless, the radii of the anisotropic vessels are relatively insensitive to the radii of the isotropic vessels. In gradient echo DSC most of the signal loss is due to static dephasing where the size of the vessels plays no role [57], as long as it is much smaller than the voxel. In our previous gradient echo DSC study, the anisotropic blood volume fraction was, therefore, assumed to be contained in only one anisotropic vessel, even though the same blood volume could be shared by more than one vessel. The present study is an extension in that it also provides an estimate of the anisotropic vessel radius. Of course, it is a simplification to assume that all vessels have the same radius. Rather, these vessels with a radius of $96.9 \mu\text{m}$ should be seen as representative of a number of vessels each with different radii and with orientations that only on average (within a given voxel) are in parallel with the WM tracts. It should also be noted that due to the pooling of voxels from various brain regions, our results are an average for WM across the entire brain. Regional variations in vascular architecture are not addressed by this approach. This, however, does not limit our general observation that the DSC signal depends on local WM fibre orientation.

Both an isotropic and an anisotropic vascular component are necessary to explain the observed changes in ΔR_2 of WM. The isotropic component results in a constant offset, whereas the anisotropic component gives rise to the orientation dependence. This finding is equivalent to our previous results for gradient echo DSC [23]. As expected, the orientation effect is much weaker in spin echo DSC than in gradient echo DSC. This observation may also explain why whole brain histograms of CBF are broader for gradient echo DSC than for spin echo DSC, and why arterial spin labelling derived CBF agrees better with spin echo DSC than with gradient echo DSC [58].

The best fit resulted in a total blood volume fraction of 2.52%, which is close to the 2.6 ml/100 g for WM tissue determined with positron emission tomography, which is considered the gold standard for CBV measurement [59]. A spin echo DSC study reported 1.3 ml/100 g for WM tissue and 4.6 ml/100 g for GM tissue, which converts approximately to 1.3% and 4.6% [60]. Using gradient echo DSC, Arakawa et al. reported a CBV of 1.44 ml/100 g in normal appearing WM and 1.86 ml/100 g in normal appearing GM of subjects with stroke [61].

The parameter maps CBF and CBV derived from ΔR_2 also show an angle dependence of about 20%, whereas the angle dependence of MTT is small. This finding is in agreement with our previous work in gradient echo DSC [23] and the notion that tissue orientation has an influence on the magnitude of the measured signal but should not have a major influence on the temporal features of the CA bolus measurement.

Myelin also gives rise to an orientation dependent signal decay [62, 63, 64]. A full 3D model that includes blood vessels, myelinated axons, and possibly ferritin would span several orders of magnitudes of length scales, making it computationally very expensive. Since the orientation-effect of myelin is small compared to the effects due to the contrast agent and also time-independent, myelin was neglected in the current study.

BOLD Contrast

The BOLD contrast and the DSC contrast are both based on the magnetic susceptibility dependent field inhomogeneities created by blood vessels. We used the vascular parameters determined with the DSC experiment for the forward calculation of the BOLD signal in WM. The gradient echo BOLD contrast showed a strong orientation dependence of 100% between parallel and perpendicular fibres at both 3 and 7 T, whereas the spin echo BOLD contrast exhibited an orientation dependence of about 20%. This finding is in agreement with the notion that spin echo fMRI has better spatial specificity than gradient echo fMRI, both for WM and GM [26, 25, 65]. Previously, the effects of tissue orientation have been described for gradient echo fMRI of cortical gray matter [22]. In cortical folds parallel to the main magnetic field, the BOLD signal was shown to be 40% higher compared to folds perpendicular to the main magnetic field [22]. However, the orientation dependence may vary between cortical layers due to intra-cortical differences in vessel architecture. Intracortical veins, which run perpendicular to the cortex, have diameters ranging between 20 and 60 μm in histological layers I, II, III and IV and 120 μm in layers V and VI [66, 67, 68]. (Note that the caliber of individual vessels increases toward the surface, but there are more smaller vessels in layers I to IV than in layers V and VI). These layer specific differences in vessel diameters suggest that spin echo BOLD signal exhibits a weaker orientation dependence in layers V and VI than in layers I to IV. Post-capillary cortical vessels, in particular pial veins on the cortical surface, in addition to the traversing veins orthogonal to the pial veins, will also have an effect on the spin echo functional MRI signal. This effect will vary with cortical orientation relative to the main magnetic field and be different for pial veins and transcortical veins [22, 66]. Moreover, the cerebrospinal fluid partly surrounding pial veins has a higher diffusion coefficient and longer T_2 than brain tissue, resulting in an increased BOLD effect from these veins [69].

Functional MRI of WM is still in its infancy [6, 9]. So far, all WM fMRI studies, including very recent work suggesting functional WM networks identified with resting state fMRI [9], have used gradient echo EPI. The dramatic WM orientation dependence of the gradient echo BOLD signal and the small spin echo BOLD effect at 3 T indicate that WM fMRI experiments should be performed at 7 T

using a spin echo sequence with echo times below 30 ms, in order to minimize orientation effects. Note, however, that this echo time is shorter than what can be attained with single shot spin echo EPI sequences, especially when high spatial resolution is desired.

We wish to emphasize that this study should not be seen as a confirmation of the WM fMRI signal being due to a BOLD effect. However, our results do indicate that, if the WM fMRI signal were due to a BOLD effect, its orientation dependency would be strong for gradient echo scans and smaller but still considerable for spin echo scans. An actual fMRI experiment for the assessment of an orientation dependence of the measured BOLD signal would be very difficult to perform for several reasons. First, there are likely regional variations in blood oxygenation changes, which impede pooling of voxels from across the entire brain. Secondly, the experiment would have to cause blood oxygenation changes across large parts of the white matter. Finally, due to the small magnitude of the BOLD effect, a large number of subjects would have to be imaged. Since the physical underpinnings are the same for DSC and BOLD fMRI, we believe that using DSC in lieu of an BOLD fMRI experiment is a valid verification of the BOLD signal's orientation dependence.

Limitations

For the simulation, several simplifications were made. The large vessels were assumed to have the same radius and to run in parallel. Furthermore, the simulated vascular tree is an accumulation of cylinders that are not connected and have no bifurcations. The blood's properties were assumed to be the same throughout the entire vasculature. We also ignored that, particularly in WM, the diffusion is anisotropic [70]. However, diffusion along the direction of a vessel does not lead to loss of coherence due to that particular vessel's magnetic field. We also ignored that the vessels themselves represent boundaries to the diffusion, since the vessels comprise only a few percent of the tissue. Moreover, there is some inherent T_2' weighting in spin echo EPI that arises from the samples acquired before and after the nominal TE. As these T_2' effects were shown to be small [71], they were not taken into account in the present study. That our simulation yielded realistic results for blood volume and CA concentration also suggests that these T_2' effects can be ignored. We also assumed that in our cohort of healthy subjects, there is no extravasation of CA. Moreover, we ignored that prior to the spin echo experiment and within the same MRI session, subjects also underwent a gradient echo DSC experiment with the administration of 0.1 mmol/kg of the same contrast agent. The minimum delay between the two injections was 7.5 minutes, allowing for baseline stabilization prior to the second bolus injection. The second ΔR_2 curve was, thus, assumed to be unaffected by the preceding experiment, though some drop in baseline MR signal intensity might

be expected. Due to the design of the study from which our data were obtained, fibre orientation was not measured using conventional DTI but by taking the $b = 0$ and $b = 2500$ scans of a diffusion kurtosis imaging sequence. However, this is unlikely to affect the results, as only the primary eigenvector from the diffusion tensor estimate had to be used for the experiment.

Conclusion

In this study, we show that the spin echo DSC experiment exhibits a strong dependence on the angle between WM tissue and the main magnetic field. In addition, we present a rapid Bloch-Torrey solution, which allows us to derive tissue parameters by fitting a model to the measured data. We show that half of the blood resides in an isotropic vascular network, and half in vessels that run, on average, in parallel with WM tissue. Simulations based on the tissue parameters determined with the DSC experiment demonstrate that the orientation dependence of the BOLD signal is 100% for gradient echo fMRI and about 20% for spin echo fMRI. The profound impact of vascular anisotropy on the BOLD and DSC signals has important implications for the interpretation of existing literature and the conduction of future experiments of fMRI and DSC in WM.

References

- [1] G. J. Bouma and J. P. Muizelaar, "Relationship between cardiac output and cerebral blood flow in patients with intact and with impaired autoregulation," *Journal of Neurosurgery*, vol. 73, pp. 368–374, Sept. 1990.
- [2] L. Østergaard, R. M. Weisskoff, D. A. Chesler, C. Gyldensted, and B. R. Rosen, "High resolution measurement of cerebral blood flow using intravascular tracer bolus passages. Part I: Mathematical approach and statistical analysis," *Magn. Reson. Med.*, vol. 36, pp. 715–725, Nov. 1996.
- [3] L. Østergaard, A. G. Sorensen, K. K. Kwong, R. M. Weisskoff, C. Gyldensted, and B. R. Rosen, "High resolution measurement of cerebral blood flow using intravascular tracer bolus passages. Part II: Experimental comparison and preliminary results," *Magn. Reson. Med.*, vol. 36, pp. 726–736, Nov. 1996.
- [4] S. Ogawa, T.-M. Lee, A. R. Kay, and D. W. Tank, "Brain magnetic resonance imaging with contrast dependent on blood oxygenation," *Proceedings of the National Academy of Sciences*, vol. 87, no. 24, pp. 9868–9872, 1990.
- [5] S. Ogawa, D. W. Tank, R. Menon, J. M. Ellermann, S. G. Kim, H. Merkle, and K. Ugurbil, "Intrinsic signal changes accompanying sensory stimulation: functional brain mapping with magnetic resonance imaging," *Proceedings of the National Academy of Sciences*, vol. 89, no. 13, pp. 5951–5955, 1992.
- [6] J. Gawryluk, E. Mazerolle, and R. D'Arcy, "Does functional mri detect activation in white matter? a review of emerging evidence, issues, and future directions," *Front Neurosci*, vol. 8, pp. 239–, 2014.
- [7] M. Fabri, G. Polonara, G. Mascioli, U. Salvolini, and T. Manzoni, "Topographical organization of human corpus callosum: an fmri mapping study," *Brain research*, vol. 1370, pp. 99–111, 2011.
- [8] L. M. Fraser, M. T. Stevens, S. D. Beyea, and R. C. D'Arcy, "White versus gray matter: fmri hemodynamic responses show similar characteristics, but differ in peak amplitude," *BMC neuroscience*, vol. 13, no. 1, p. 91, 2012.
- [9] M. Peer, M. Nitzan, A. Bick, N. Levin, and S. Arzy, "Evidence for functional networks within the human brain's white matter," *J Neurosci*, vol. 37, no. 27, pp. 6394–6407, 2017.
- [10] G. C. Petzold and V. N. Murthy, "Role of astrocytes in neurovascular coupling," *Neuron*, vol. 71, no. 5, pp. 782–797, 2011.
- [11] A. J. Smith, H. Blumenfeld, K. L. Behar, D. L. Rothman, R. G. Shulman, and F. Hyder, "Cerebral energetics and spiking frequency: the neurophysiological basis of fmri," *Proceedings of the National Academy of Sciences*, vol. 99, no. 16, pp. 10765–10770, 2002.
- [12] P. Barbaresi, M. Fabri, and E. Mensà, "Characterization of no-producing neurons in the rat corpus callosum," *Brain and behavior*, vol. 4, no. 3, pp. 317–336, 2014.
- [13] A. Rauscher, J. Sedlacik, M. Barth, E. M. Haacke, and J. R. Reichenbach, "Noninvasive assessment of vascular architecture and function during modulated blood oxygenation using susceptibility weighted magnetic resonance imaging," *Magnetic resonance in medicine*, vol. 54, no. 1, pp. 87–95, 2005.
- [14] H. Nonaka, M. Akima, T. Hatori, T. Nagayama, Z. Zhang, and F. Ihara, "Microvasculature of the human cerebral white matter: Arteries of the deep white matter," *Neuropathology*, vol. 23, pp. 111–118, June 2003.
- [15] H. Nonaka, M. Akima, T. Hatori, T. Nagayama, Z. Zhang, and F. Ihara, "The microvasculature of the cerebral white matter: arteries of the subcortical white matter," *J. Neuropathol. Exp. Neurol.*, vol. 62, pp. 154–161, Feb. 2003.
- [16] T. Okudera, Y. P. Huang, A. Fukusumi, Y. Nakamura, J. Hatazawa, and K. Uemura, "Micro-angiographical studies of the medullary venous system of the cerebral hemisphere," *Neuropathology*, vol. 19, pp. 93–111, Jan. 1999.
- [17] M. Cavaglia, S. M. Dombrowski, J. Drazba, A. Vasanji, P. M. Bokesch, and D. Janigro, "Regional variation in brain capillary density and vascular response to ischemia," *Brain Research*, vol. 910, pp. 81–93, Aug. 2001.
- [18] K. Cai, R. Tain, S. Das, F. C. Damen, Y. Sui, T. Valyi-Nagy, M. A. Elliott, and X. J. Zhou, "The feasibility of quantitative MRI of perivascular spaces at 7 T," *Journal of Neuroscience Methods*, vol. 256, pp. 151–156, Dec. 2015.
- [19] A. Deistung, A. Rauscher, J. Sedlacik, J. Stadler, S. Witoszynskyj, and J. R. Reichenbach, "Susceptibility weighted imaging at ultra high magnetic field strengths: Theoretical considerations and experimental results," *Magn. Reson. Med.*, vol. 60, pp. 1155–1168, Nov. 2008.
- [20] J. R. Reichenbach and E. M. Haacke, "High-resolution BOLD venographic imaging: a window into brain function," *NMR Biomed.*, vol. 14, pp. 453–467, Nov. 2001.
- [21] C. Denk and A. Rauscher, "Susceptibility weighted imaging with multiple echoes," *J. Magn. Reson. Imaging*, vol. 31, pp. 185–191, Jan. 2010.
- [22] L. Gagnon, S. Sakadžić, F. Lesage, J. J. Musacchia, J. Lefebvre, Q. Fang, M. A. Yücel, K. C. Evans, E. T. Mandeville, J. Cohen-Adad, J. R. Polimeni, M. A. Yaseen, E. H. Lo, D. N. Greve, R. B. Buxton, A. M. Dale, A. Devor, and D. A. Boas, "Quantifying the Microvascular Origin of BOLD-fMRI from First Principles with Two-Photon Microscopy and an Oxygen-Sensitive Nanoprobe," *J Neurosci*, vol. 35, pp. 3663–3675, Feb. 2015.
- [23] E. Hernández-Torres, N. Kassner, N. D. Forkert, L. Wei, V. Wiggermann, M. Daemen, L. Machan, A. Traboulsee, D. Li, and A. Rauscher, "Anisotropic cerebral vascular architecture causes orientation dependency in cerebral blood flow and volume measured with dynamic susceptibility contrast magnetic resonance imaging," *J Cereb Blood Flow Metab*, p. 0271678X16653134, June 2016.

- [24] J. L. Boxerman, L. M. Hamberg, B. R. Rosen, and R. M. Weisskoff, "MR contrast due to intravascular magnetic susceptibility perturbations," *Magn Reson Med*, vol. 34, pp. 555–566, Oct. 1995.
- [25] K. Uludağ, B. Müller-Bierl, and K. Ugurbil, "An integrative model for neuronal activity-induced signal changes for gradient and spin echo functional imaging. uludağ k1, müller-bierl b, uğurbil k.," *Neuroimage*, vol. 48, no. 1, pp. 150–165, 2009.
- [26] D. Norris, "Spin-echo fmri: The poor relation?," *Neuroimage*, vol. 15, pp. 1109–1115, 2012.
- [27] K. Uludağ and P. Blinder, "Linking brain vascular physiology to hemodynamic response in ultra-high field mri," *NeuroImage*, 2017.
- [28] W. Meier-Ruge, O. Hunziker, U. Schulz, H. J. Tobler, and A. Schweizer, "Stereological changes in the capillary network and nerve cells of the aging human brain," *Mechanisms of Ageing and Development*, vol. 14, pp. 233–243, Sept. 1980.
- [29] J. P. Marques and R. W. Bowtell, "Using forward calculations of the magnetic field perturbation due to a realistic vascular model to explore the BOLD effect," *NMR Biomed.*, vol. 21, pp. 553–565, July 2008.
- [30] H. C. Torrey, "Bloch Equations with Diffusion Terms," *Phys. Rev.*, vol. 104, pp. 563–565, Nov. 1956.
- [31] G. C. Wick, "Properties of Bethe-Salpeter Wave Functions," *Phys. Rev.*, vol. 96, pp. 1124–1134, Nov. 1954.
- [32] C. H. Ziener, S. Glutsch, P. M. Jakob, and W. R. Bauer, "Spin dephasing in the dipole field around capillaries and cells: Numerical solution," *Phys. Rev. E*, vol. 80, p. 046701, Oct. 2009.
- [33] C. H. Ziener, T. Kampf, G. Reents, H.-P. Schlemmer, and W. R. Bauer, "Spin dephasing in a magnetic dipole field," *Phys. Rev. E*, vol. 85, p. 051908, May 2012.
- [34] R. Guardiola, "Monte carlo methods in quantum many-body theories," in *Microscopic Quantum Many-Body Theories and Their Applications*, Lecture Notes in Physics, pp. 269–336, Springer, Berlin, Heidelberg, 1998. DOI: 10.1007/BFb0104529.
- [35] P. Bader, S. Blanes, and F. Casas, "Solving the Schrödinger eigenvalue problem by the imaginary time propagation technique using splitting methods with complex coefficients," *The Journal of Chemical Physics*, vol. 139, p. 124117, Sept. 2013.
- [36] D. V. Nguyen, J.-R. Li, D. Grebenkov, and D. Le Bihan, "A finite elements method to solve the Bloch–Torrey equation applied to diffusion magnetic resonance imaging," *Journal of Computational Physics*, vol. 263, pp. 283–302, Apr. 2014.
- [37] T. S. Ursell, "The Diffusion Equation A Multi-dimensional Tutorial," *California Institute of Technology, Pasadena, Tech. Rep*, 2007.
- [38] M. Holz, S. R. Heil, and A. Sacco, "Temperature-dependent self-diffusion coefficients of water and six selected molecular liquids for calibration in accurate 1h NMR PFG measurements," *Phys. Chem. Chem. Phys.*, vol. 2, pp. 4740–4742, Jan. 2000.
- [39] W. E. Schiesser, *The numerical method of lines: integration of partial differential equations*. Elsevier, 2012.
- [40] C. Moler and C. Van Loan, "Nineteen Dubious Ways to Compute the Exponential of a Matrix," *SIAM Rev.*, vol. 20, pp. 801–836, Oct. 1978.
- [41] M. Caliari, P. Kandol, A. Ostermann, and S. Rainer, *Comparison of various methods for computing the action of the matrix exponential*. submitted.
- [42] C. Moler and C. Van Loan, "Nineteen Dubious Ways to Compute the Exponential of a Matrix, Twenty-Five Years Later," *SIAM Rev.*, vol. 45, pp. 3–49, Jan. 2003.
- [43] A. Al-Mohy and N. Higham, "Computing the Action of the Matrix Exponential, with an Application to Exponential Integrators," *SIAM J. Sci. Comput.*, vol. 33, pp. 488–511, Jan. 2011.
- [44] MATLAB, *version 8.6 (R2015b), Optimization Toolbox version 7.3*. Natick, Massachusetts: The MathWorks Inc., 2015.
- [45] H. An and W. Lin, "Cerebral venous and arterial blood volumes can be estimated separately in humans using magnetic resonance imaging," *Magnetic resonance in medicine*, vol. 48, no. 4, pp. 583–588, 2002.
- [46] V. Pollard, D. S. Prough, A. E. DeMelo, D. J. Deyo, T. Uchida, and H. F. Stoddart, "Validation in volunteers of a near-infrared spectroscope for monitoring brain oxygenation in vivo," *Anesthesia & Analgesia*, vol. 82, no. 2, pp. 269–277, 1996.
- [47] J. M. Zhao, C. S. Clingman, M. J. Närväinen, R. A. Kauppinen, and P. C. van Zijl, "Oxygenation and hematocrit dependence of transverse relaxation rates of blood at 3t," *Magn. Reson. Med.*, vol. 58, pp. 592–597, Sept. 2007.
- [48] E. Yacoub, A. Shmuel, J. Pfeuffer, V. De Moortele, G. Adriany, P. Andersen, J. T. Vaughan, H. Merkle, K. Ugurbil, X. Hu, et al., "Imaging brain function in humans at 7 tesla," *Magnetic Resonance in Medicine*, vol. 45, no. 4, pp. 588–594, 2001.
- [49] B. Hansen, T. E. Lund, R. Sangill, and S. N. Jespersen, "Experimentally and computationally fast method for estimation of a mean kurtosis," *Magn Reson Med*, vol. 69, pp. 1754–1760, June 2013.
- [50] M. Jenkinson, C. F. Beckmann, T. E. J. Behrens, M. W. Woolrich, and S. M. Smith, "FSL," *NeuroImage*, vol. 62, pp. 782–790, Aug. 2012.
- [51] E. Hernández-Torres, V. Wiggermann, S. Hametner, T. R. Baumeister, A. D. Sadovnick, Y. Zhao, L. Machan, D. K. B. Li, A. Traboulsee, and A. Rauscher, "Orientation Dependent MR Signal Decay Differentiates between People with MS, Their Asymptomatic Siblings and Unrelated Healthy Controls," *PLOS ONE*, vol. 10, p. e0140956, Oct. 2015.
- [52] K. Mouridsen, F. K., H. N., G. L., O. L., and K. S., "Bayesian estimation of cerebral perfusion using a physiological model of microvasculature," *Neuroimage*, vol. 22, pp. 570–579, 2006.
- [53] K. Mouridsen, M. B. Hansen, L. Østergaard, and S. N. Jespersen, "Reliable estimation of capillary transit time distributions using DSC-MRI," *J Cereb Blood Flow Metab*, vol. 34, pp. 1511–1521, Sept. 2014.
- [54] J. Sedlacik, A. Rauscher, and J. R. Reichenbach, "Obtaining blood oxygenation levels from mr signal behavior in the presence of single venous vessels," *Magnetic resonance in medicine*, vol. 58, no. 5, pp. 1035–1044, 2007.
- [55] D. S. Grebenkov, "Laplacian eigenfunctions in NMR. I. A numerical tool," *Concepts Magn. Reson.*, vol. 32A, pp. 277–301, July 2008.
- [56] T. H. Jochimsen, D. Ivanov, D. V. M. Ott, W. Heinke, R. Turner, H. E. Möller, and J. R. Reichenbach, "Whole-brain mapping of venous vessel size in humans using the hypercapnia-induced BOLD effect," *NeuroImage*, vol. 51, pp. 765–774, June 2010.
- [57] D. A. Yablonskiy and E. M. Haacke, "Theory of NMR signal behavior in magnetically inhomogeneous tissues: The static dephasing regime," *Magn. Reson. Med.*, vol. 32, pp. 749–763, Dec. 1994.
- [58] A. M. Wong, F.-X. Yan, and H.-L. Liu, "Comparison of three-dimensional pseudo-continuous arterial spin labeling perfusion imaging with gradient-echo and spin-echo dynamic susceptibility contrast MRI," *J. Magn. Reson. Imaging*, vol. 39, pp. 427–433, Feb. 2014.
- [59] K. L. Leenders, D. Perani, A. A. Lammertsma, J. D. Heather, P. Buckingham, M. J. Healy, J. M. Gibbs, R. J. Wise, J. Hatazawa, and S. Herold, "Cerebral blood flow, blood volume and oxygen utilization. Normal values and effect of age," *Brain*, vol. 113 (Pt 1), pp. 27–47, Feb. 1990.
- [60] J. Helenius, J. Perkiö, L. Soinne, L. Østergaard, R. A. D. Carano, O. Salonen, S. Savolainen, M. Kaste, H. J. Aronen,

and T. Tatlisumak, “Cerebral Hemodynamics in a Healthy Population Measured by Dynamic Susceptibility Contrast Mr Imaging,” *Acta Radiologica*, vol. 44, pp. 538–546, Jan. 2003.

- [61] S. Arakawa, P. M. Wright, M. Koga, T. G. Phan, D. C. Reutens, I. Lim, M. R. Gunawan, H. Ma, N. Perera, J. Ly, J. Zavala, G. Fitt, and G. A. Donnan, “Ischemic Thresholds for Gray and White Matter,” *Stroke*, vol. 37, pp. 1211–1216, May 2006.
- [62] C. Denk, E. H. Torres, A. MacKay, and A. Rauscher, “The influence of white matter fibre orientation on MR signal phase and decay,” *NMR Biomed.*, vol. 24, pp. 246–252, Apr. 2011.
- [63] J. Lee, P. van Gelderen, L.-W. Kuo, H. Merkle, A. C. Silva, and J. H. Duyn, “T2*-based fiber orientation mapping,” *Neuroimage*, vol. 57, pp. 225–234, July 2011.
- [64] S. Wharton and R. Bowtell, “Fiber orientation-dependent white matter contrast in gradient echo MRI,” *Proc Natl Acad Sci U S A*, vol. 109, pp. 18559–18564, Nov. 2012.
- [65] S. Lee, A. Silva, S. Ugurbil, and S. Kim, “Diffusion-weighted spin-echo fmri at 9.4 t: microvascular/tissue contribution to bold signal changes,” *Magn Reson Med*, vol. 42, no. 5, pp. 919–28, 1999.
- [66] I. Markuerkiaga, M. Barth, and D. Norris, “A cortical vascular model for examining the specificity of the laminar bold signal,” *Neuroimage*, vol. 132, pp. 491–498, 2016.
- [67] B. Weber, A. L. Keller, J. Reichold, and N. K. Logothetis, “The microvascular system of the striate and extrastriate visual cortex of the macaque,” *Cerebral cortex*, vol. 18, no. 10, pp. 2318–2330, 2008.
- [68] H. M. Duvernoy, S. Delon, and J. Vannson, “Cortical blood vessels of the human brain,” *Brain research bulletin*, vol. 7, no. 5, pp. 519–579, 1981.
- [69] D. Pflugfelder, K. Vahedipour, K. Uludağ, N. J. Shah, and T. Stöcker, “On the numerically predicted spatial bold fmri specificity for spin echo sequences,” *Magnetic resonance imaging*, vol. 29, no. 9, pp. 1195–1204, 2011.
- [70] C. Beaulieu and P. S. Allen, “Determinants of anisotropic water diffusion in nerves,” *Magn. Reson. Med.*, vol. 31, pp. 394–400, Apr. 1994.
- [71] T. Q. Duong, E. Yacoub, G. Adriany, X. Hu, K. Ugurbil, and S.-G. Kim, “Microvascular BOLD contribution at 4 and 7 T in the human brain: Gradient-echo and spin-echo fMRI with suppression of blood effects,” *Magn. Reson. Med.*, vol. 49, pp. 1019–1027, June 2003.
- [72] I. Markuerkiaga, M. Barth, and D. G. Norris, “A cortical vascular model for examining the specificity of the laminar BOLD signal,” *NeuroImage*, vol. 132, pp. 491–498, May 2016.

Acknowledgements

This work was funded by the Natural Sciences and Engineering Research Council (016-05371) of Canada and the National Multiple Sclerosis Society (RG-1507-05301). AR is funded by Canada Research Chairs. JD was funded by NSERC.

Data and Code Availability

All raw data and code are available from the authors upon request. The framework for the solution of the Bloch-Torrey equation will be made available on our website.

Author Contributions

JD: data analysis, numerical simulations, interpretation of results, writing of manuscript; LW: numerical simulations; EHT: data analysis; CK: numerical simulations; NDF: interpretation of results; RA, TEL, and BH: data acquisition and interpretation of results; AR: idea, study supervision, interpretation of results, writing of manuscript; all authors contributed to the editing of the manuscript.

Figures and Tables

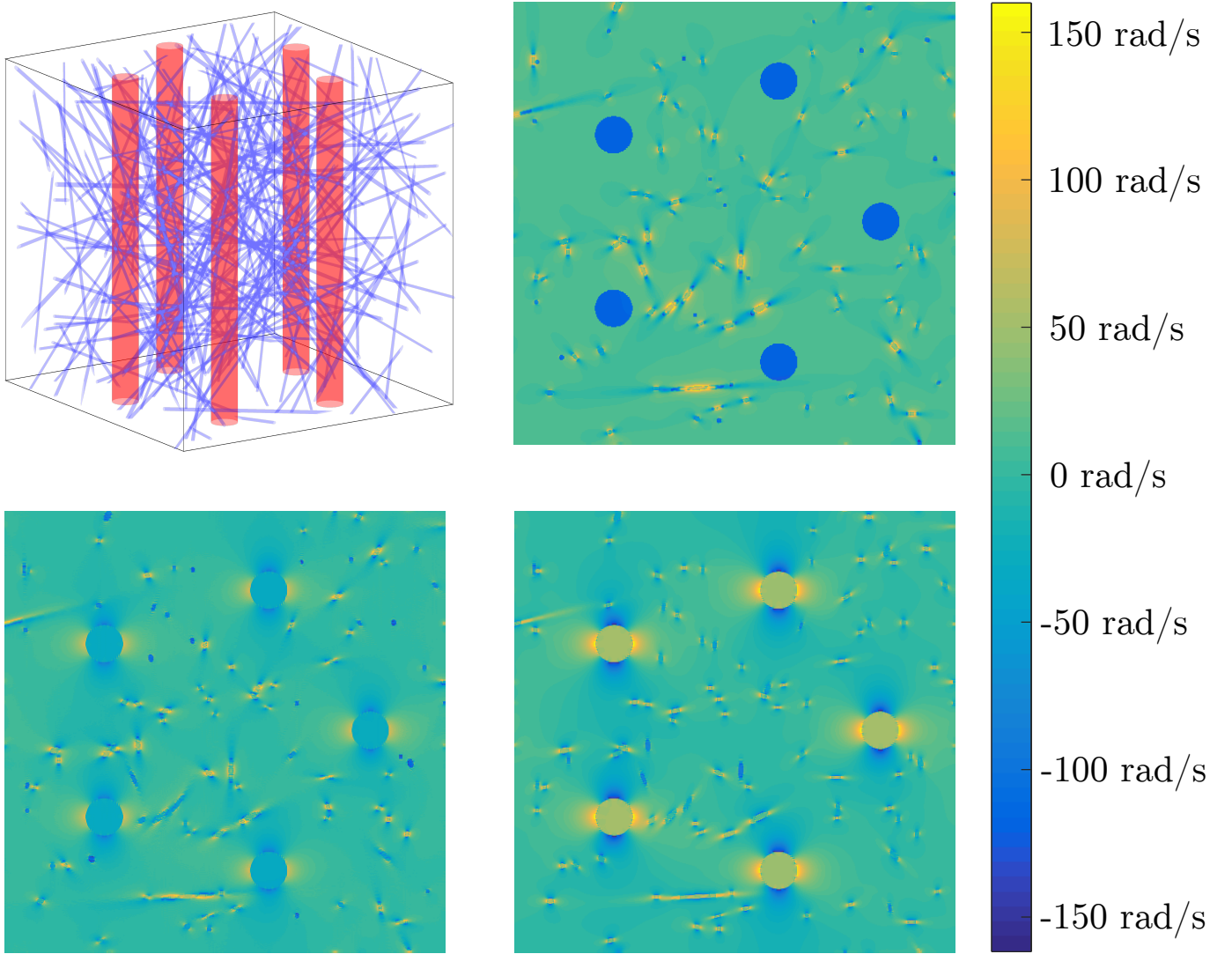


Figure 1: The top-left figure shows an example voxel geometry. The $3 \times 3 \times 3 \text{ mm}^3$ voxel is populated with an isotropic vascular bed and $L = 5$ anisotropic large vessels in the z -direction. The total volume occupied by the blood vessels is determined by the blood volume fraction BVF. The relative fraction of blood contained in the isotropic vascular bed is determined by the isotropic relative blood volume fraction iRBVF, and the amount of blood contained in the anisotropic vessels is then $\text{aRBVF} = 1 - \text{iRBVF}$. The magnetic field generated by this configuration is computed by the convolution of the susceptibility map with the unit dipole kernel. Example cross-sections of the frequency shift map $\delta\omega$ are shown for $\alpha = 0^\circ$ (top right), 45° (bottom left), and 90° (bottom right). It can be easily observed that near large vessels, the resonance frequency (i.e. the magnetic field) remains locally relatively constant compared to the resonance frequency near small vessels, which changes rapidly over short distances. Note also the increase in strength and range of inhomogeneities around the large anisotropic vessels as α increases, introducing the dependence on the angle α into the simulations.

Magnetization Propagation Algorithm

```
1: Initialize:  $\mathcal{M}_0 := i, \Delta t := \text{TE}/30, k := 0$ 
2: while  $k\Delta t < \text{TE}$  do
3:    $\mathcal{M}_{k+\frac{1}{2}} := e^{-\Gamma(\mathbf{r})\Delta t} \mathcal{M}_k$ 
4:    $\mathcal{M}_{k+1} := \Phi(\mathbf{r}, \Delta t) * \mathcal{M}_{k+\frac{1}{2}}$ 
5:   if  $(k+1)\Delta t = \text{TE}/2$  then
6:      $\mathcal{M}_{k+1} := \overline{\mathcal{M}}_{k+1}$ 
7:   end if
8:    $k := k + 1$ 
9: end while
10:  $S(\text{TE}) := \int \mathcal{M}_k d^3\mathbf{r}$ 
```

Algorithm 1: Magnetization propagation algorithm used to simulate the signal $S(\text{TE})$ for a given set of free parameters CA_{PEAK} , BVF , iBVF , and L . All four free parameters are encoded solely in the complex decay rate $\Gamma(\mathbf{r})$; the rest of the algorithm does not depend on them. The notation \mathcal{M}_ν is shorthand for $\mathcal{M}(\mathbf{r}, \nu\Delta t)$ throughout the algorithm. If the $\mathcal{O}(\Delta t^3)$ order evolution equation 11 were used instead, line 3 should be modified to decay for only a half time step $\Delta t/2$, line 4 should perform the Gaussian convolution in-place, and an extra line should be added directly following the convolution which decays for another half time step $\Delta t/2$.

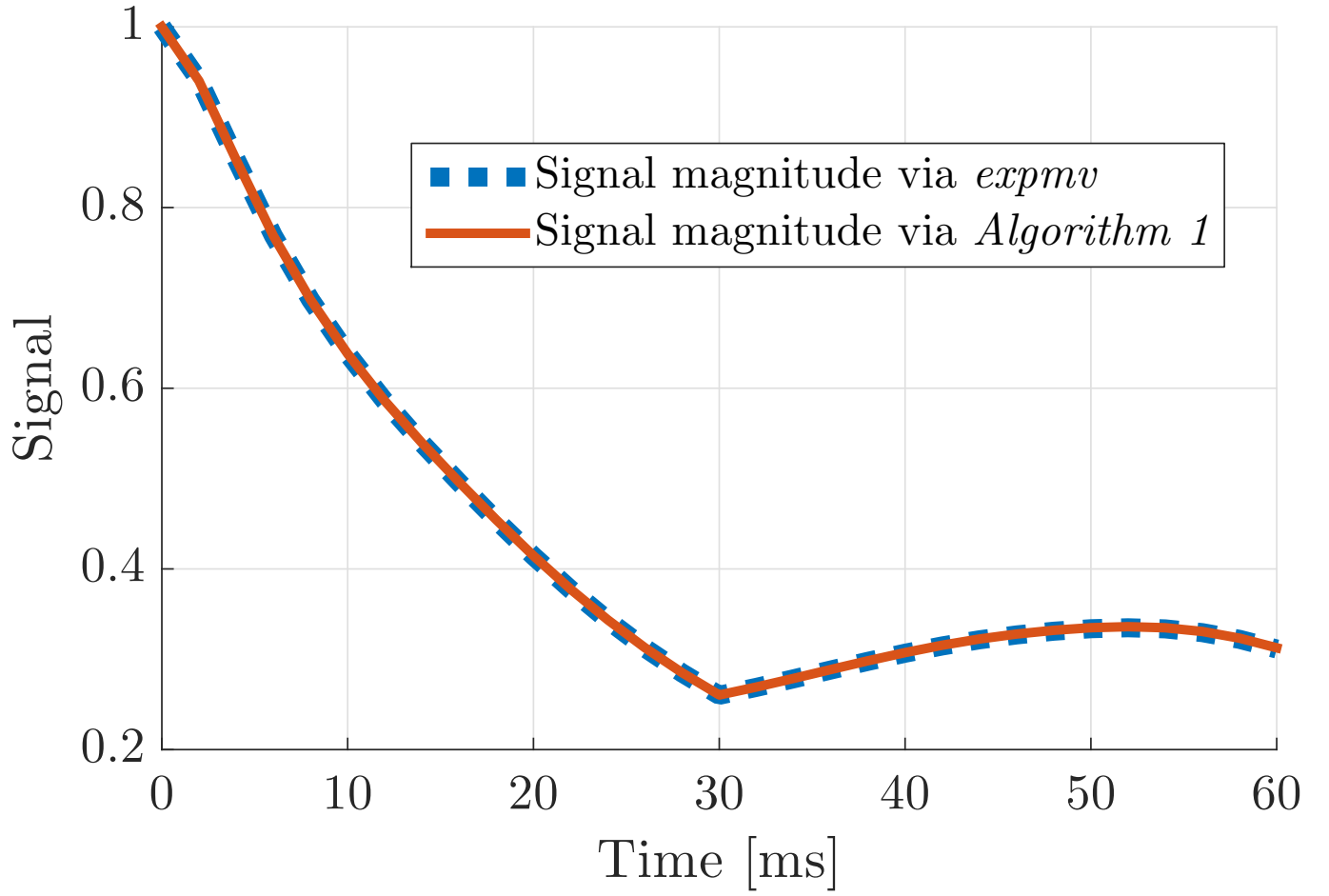


Figure 2: Comparison between solving the Bloch-Torrey equation exactly using the method of lines in conjunction with Higham’s *expmv* integrator [43], and solving the Bloch-Torrey equation approximately using the two-step approximate solution as described in Algorithm 1. The signal decay through time calculation shows strong agreement between the two methods, with error values of 0.064% +/- 0.045%; the maximum error value of 0.14% occurs at 60 ms.

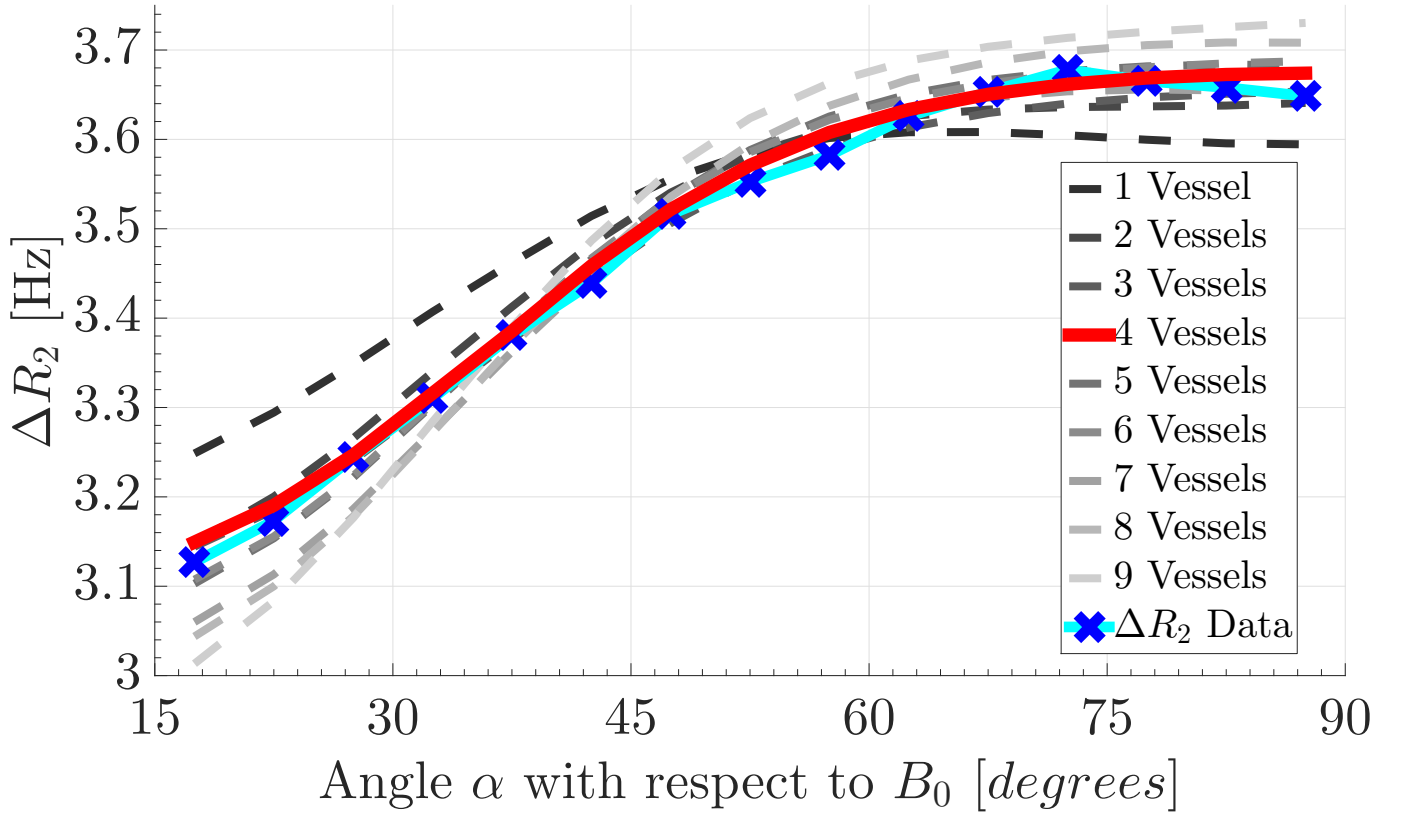


Figure 3: ΔR_2 vs. α (blue) and fitted model (red) for $L = 4$ anisotropic blood vessels. ΔR_2 was 20% larger for fibres perpendicular to the main magnetic field compared to parallel fibres. The resulting parameters found are $CA_{\text{PEAK}} = 6.39 \text{ mM}$, $BVF = 2.52\%$, and $iRBVF = 46.8\%$, corresponding to 1.18% of cerebral blood in isotropic vasculature and 1.34% in anisotropic vasculature. It should be noted that $>97\%$ of data points have an angle with B_0 greater than 15° . For angles below 15° , there was an upward trend that may be an artifact of the small number of voxels contributing to these angles. This trend was not observed in the gradient echo EPI experiment [23], nor in the simulations of this study, and therefore these points were excluded for the purposes of parameter fitting.

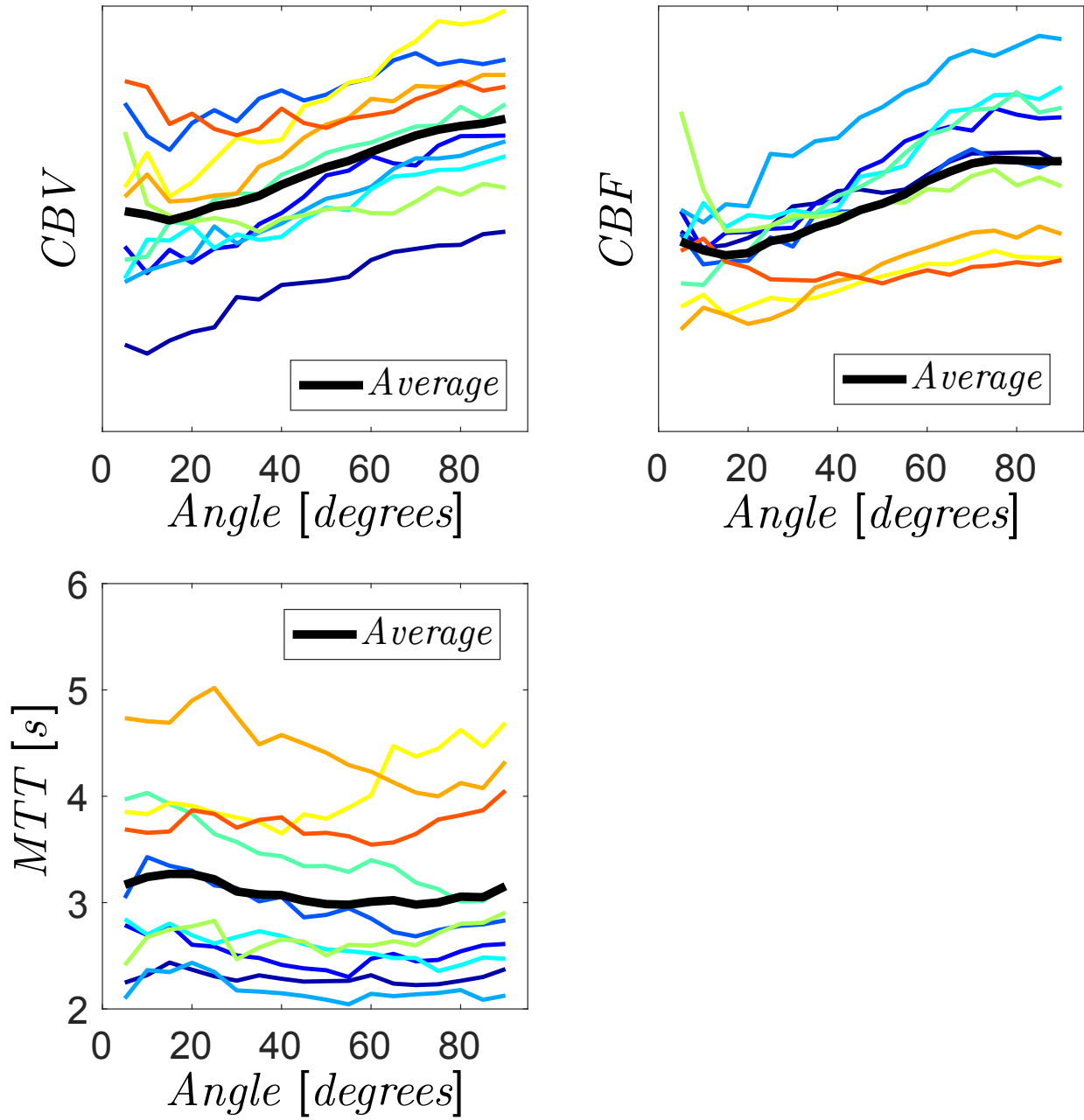


Figure 4: CBV and CBF exhibit larger values at 90° compared to 0°. The orientation dependence of MTT is weak. Coloured curves represent individual subjects. As no normalization of CBV and CBF to an internal reference tissue was performed, both CBV and CBF are given in arbitrary units, which were normalized to the average from zero to five degrees.

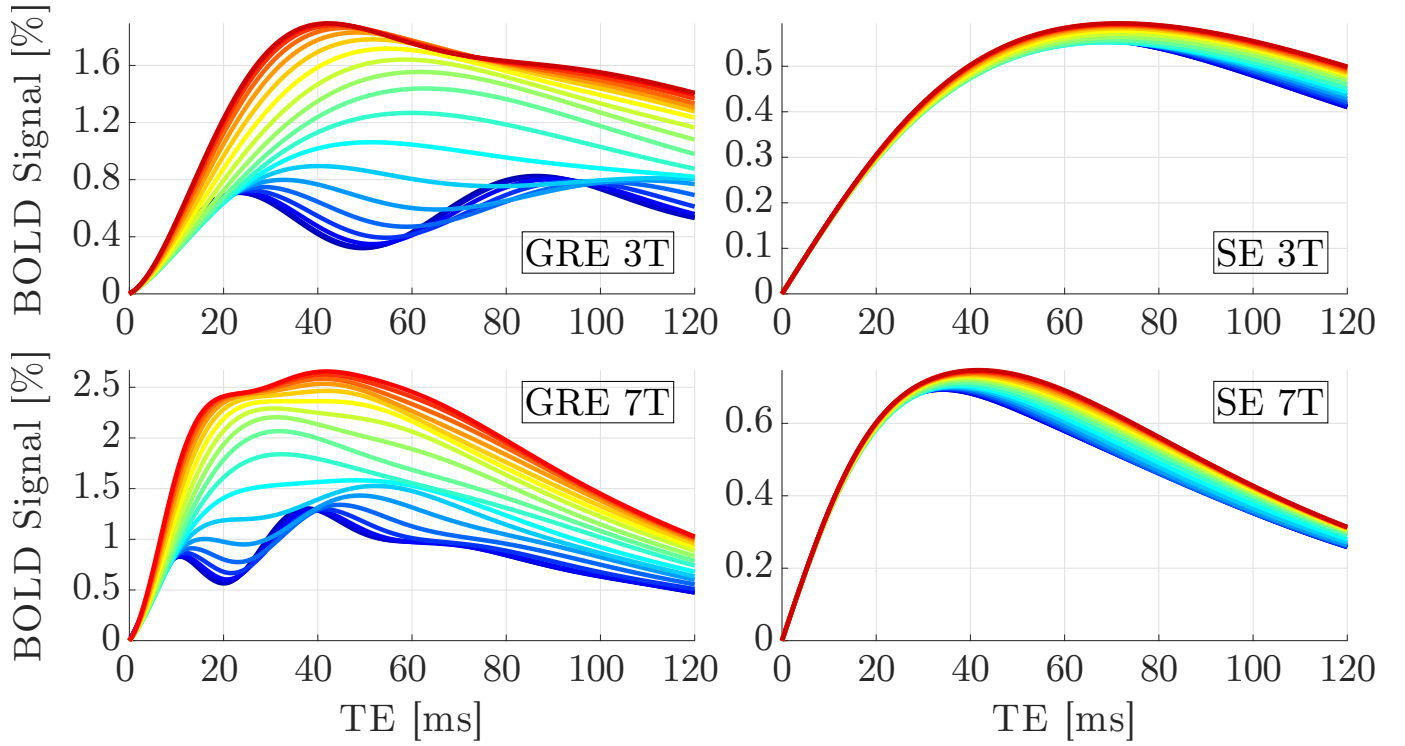


Figure 5: The WM BOLD signal for gradient echo (left) and spin echo (right) fMRI at 3 T (top) and 7 T (bottom). The gradient echo signal exhibits a strong angle dependence of up to 100% for for echo times between 25 and 60 ms, whereas in the spin echo angle dependence does not exceed 20%. Since the spin echo angle dependence is diffusion mediated, it does not become relevant until 40 ms. The colours represent fibre orientations ranging from 0° (dark blue) to 90° (dark red). Note that the BOLD contrasts are not scaled for field strength.

Supplemental Materials

Using MR vessel size imaging, Jochimsen and colleagues reported radii of $13.7\mu\text{m}$ with a standard deviation of $2.1\mu\text{m}$ [56]. Additional experiments were performed with these parameters to see what effects doubling of the capillary radius has on the results. All other factors held constant, the fit to the perfusion orientation experiment was performed to determine vascular parameters, followed by the simulated BOLD experiment, as was done for the case of the smaller $7\mu\text{m}$ radius minor vasculature and described in the manuscript.

The results of the fit to the perfusion experiment in Figure S1 illustrate the robustness of the fit parameters to changes in vessel sizing. While the total blood volume fraction BVF increases, the increase is almost entirely due to increased isotropic blood (from 1.18% to 2.30%). The anisotropic blood fraction decreases slightly from 1.34% to 1.19%.

This increase in isotropic blood volume is expected due to the fact that diffusion mediated spin dephasing is sensitive to local magnetic field gradients, which are weaker in the case of larger minor vessels. This results in a larger fraction of blood being required to produce the same (orientation independent-) change in R_2 when compared to isotropic vasculature that consists of smaller vessels.

The differing anisotropic blood volume fractions is partly due to the differing number of optimal vessels L . In fact, the optimal anisotropic BVF for the $7\mu\text{m}$ experiment corresponding to $L = 5$ was 1.28%. The anisotropic BVF is therefore relatively independent of the minor vasculature, as is expected when the cause of the orientation dependency is strictly due to the anisotropic blood, and not the isotropic blood. Note that the total blood volume computed with $7\mu\text{m}$ experiment (2.52%) is very close to the blood volume determined with positron emission tomography (2.6%), whereas the $13.7\mu\text{m}$ experiment results in a blood volume that is much larger at 3.5%.

The remaining variable parameter, the contrast agent concentration, was relatively independent of minor vessel size as well. The $7\mu\text{m}$ experiment found CA values of 6.39 mM for $L = 4$ anisotropic vessels and 6.30 mM for $L = 5$ vessels, compared with 6.23 mM for $L = 5$ vessels for the $13.7\mu\text{m}$ experiment.

Lastly, the strength and orientation of the BOLD signals in Figure S2 calculated at 3T and 7T for SE and GRE scans were consistent as well. The peak strength of the BOLD signals all decreased approximately proportional to the change in total BVF ($2.52\%/3.49\% = 0.722$, or roughly two-thirds to three-quarters). The orientation dependency of the SE BOLD signal is the same as in the $7\mu\text{m}$ experiment; the GRE BOLD signal orientation dependency is weaker.

In summary, the parameters of interest (anisotropic blood volume and the BOLD effect) are relatively insensitive to changes in microvascular parameters.

Supplemental Figures

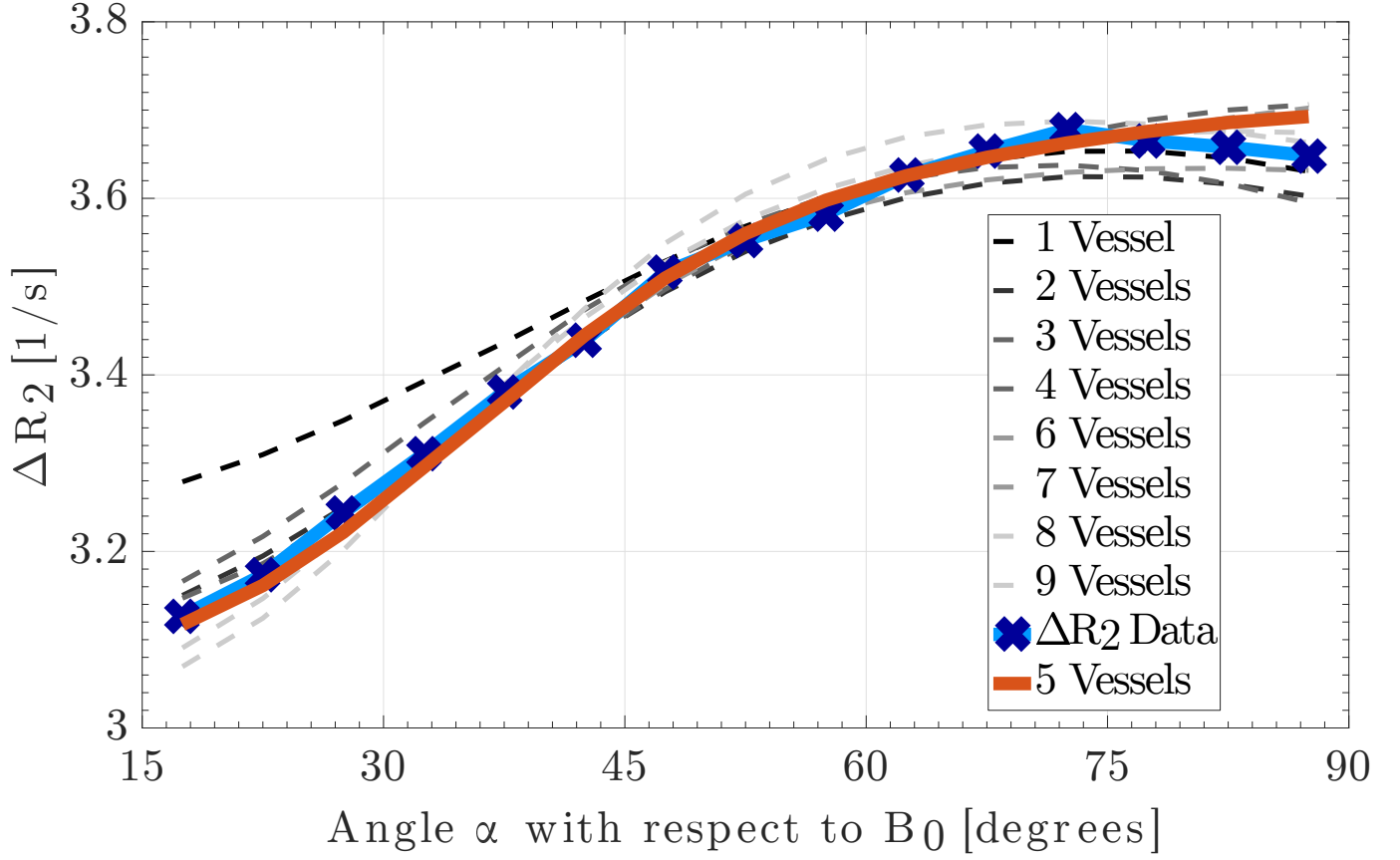


Figure S1: ΔR_2 vs. α (blue) and fitted model (red) for $L = 5$ anisotropic blood vessels. ΔR_2 was 20% larger for fibres perpendicular to the main magnetic field compared to parallel fibres. The resulting parameters found are $CA_{PEAK} = 6.23 \text{ mM}$, $BVF = 3.49\%$, and $iRBVF = 65.9\%$, corresponding to 2.30% of cerebral blood in isotropic vasculature and 1.19% in anisotropic vasculature. It should be noted that $>97\%$ of data points have an angle with B_0 greater than 15° . For angles below 15° , there was an upward trend that may be an artifact of the small number of voxels contributing to these angles. This trend was not observed in the gradient echo EPI experiment [23], nor in the simulations of this study, and therefore these points were excluded for the purposes of parameter fitting.

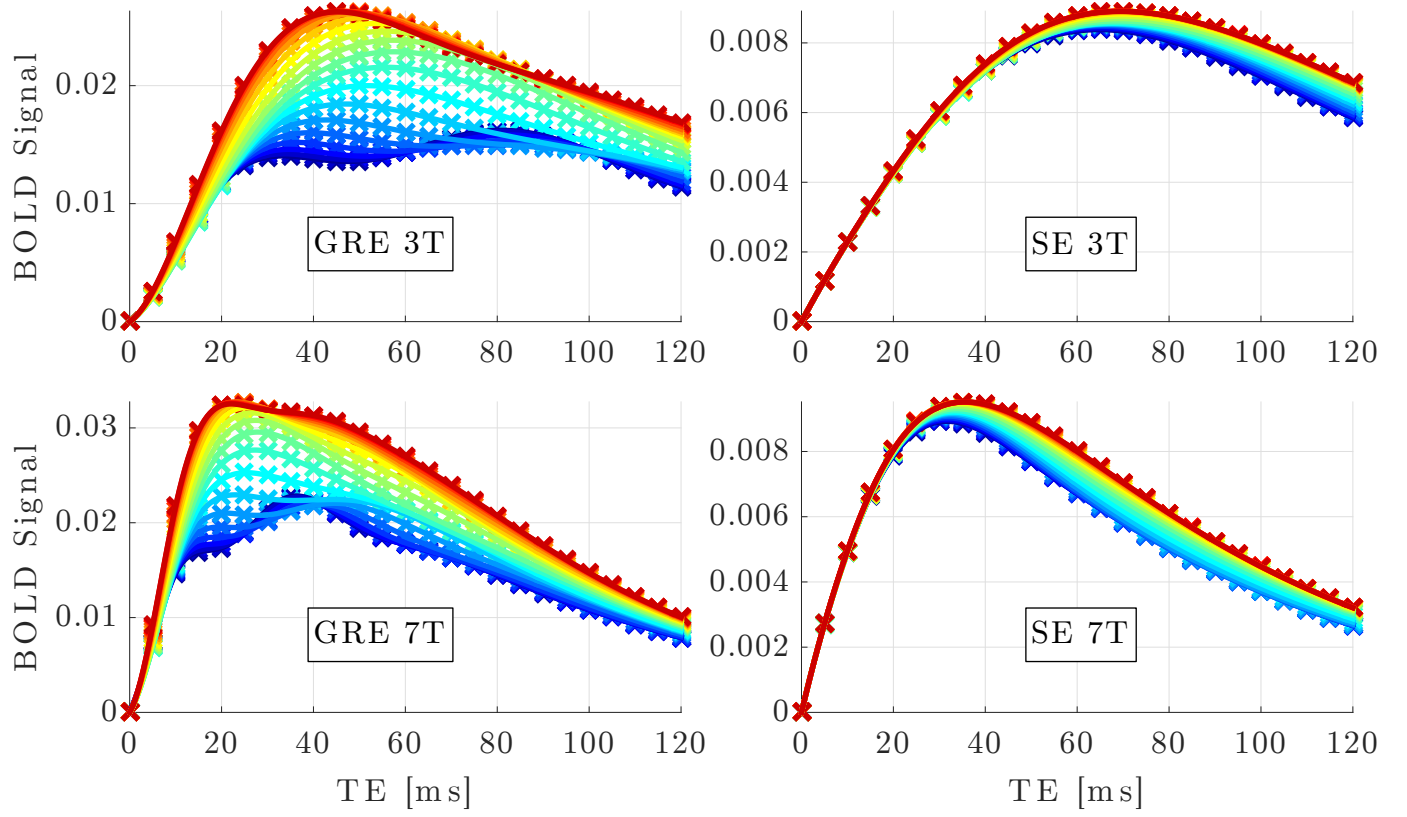


Figure S2: The WM BOLD signal for gradient echo (left) and spin echo (right) fMRI at 3T (top) and 7T (bottom). The gradient echo signal exhibits a strong angle dependence of up to 100% for for echo times between 25 and 60 ms, whereas in the spin echo angle dependence does not exceed 20%. Since the spin echo angle dependence is diffusion mediated, it does not become relevant until 40 ms. The colours represent fibre orientations ranging from 0° (dark blue) to 90° (dark red). Note that the BOLD contrasts are not scaled for field strength.



Figure S3, For Review Only: Soft X-ray picture of the cerebral hemisphere. Many arterial branches terminate in the cortex and subcortical white matter. Some large arteries run in straight lines centripetally toward the lateral ventricle. No centrifugal arteries are noted. (This figure and its capture were taken from Nonaka et al. *Neuropathology* 2003, 23, 111-118 [15].)

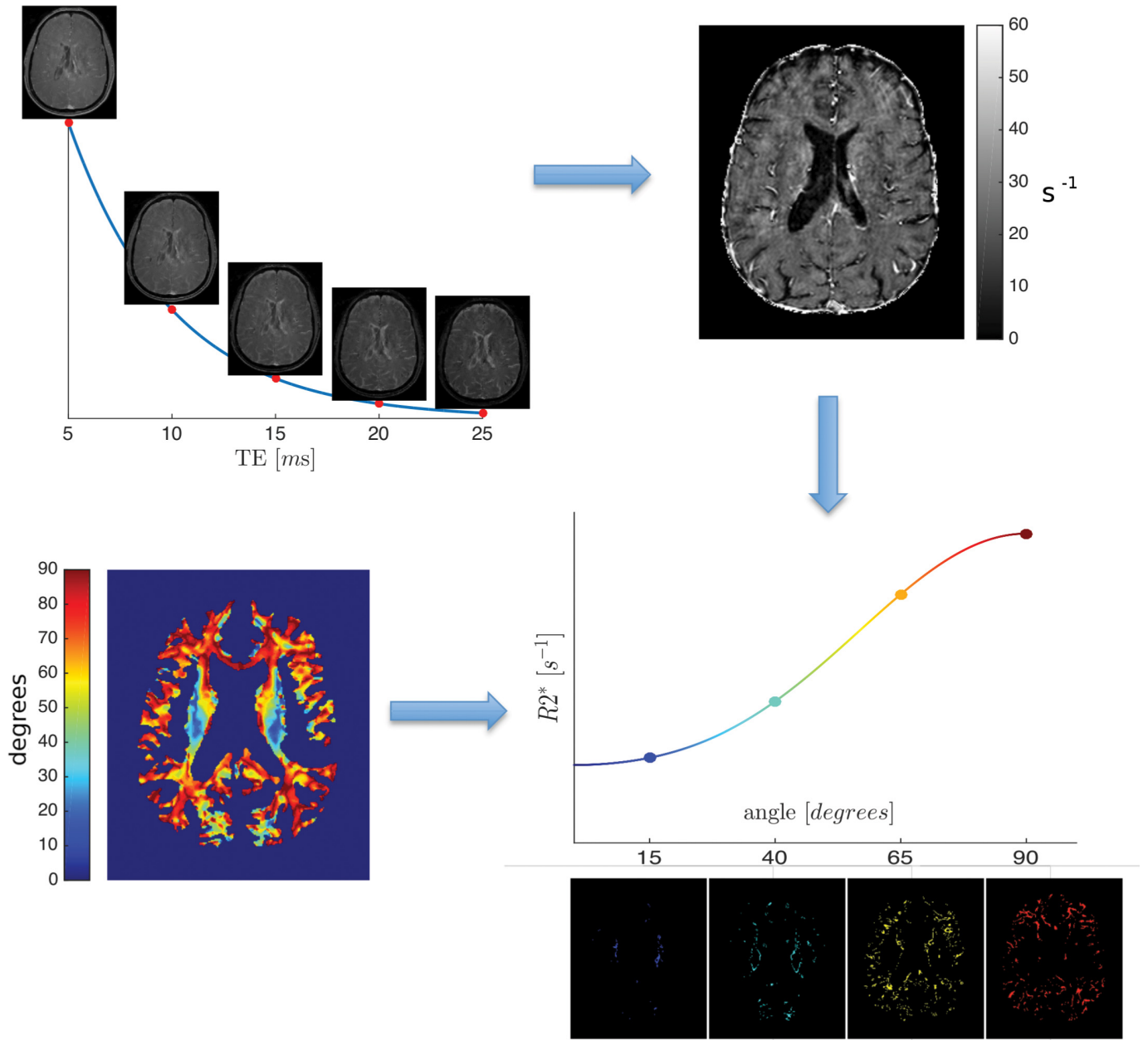


Figure S4, For Review Only: Data processing workflow for orientation mapping. The angle between the largest eigenvector of the diffusion tensor and B_0 is computed in each voxel. The quantitative image values (in this image it is R_2^* ; for the present perfusion data it is ΔR_2) from each orientation interval are pooled together, averaged and then plotted against the corresponding orientation. The four exemplary images below the R_2^* curve represent four angle intervals (10–15, 35–40, 60–65, and 85–90 degrees, respectively) and show which voxels contribute to the R_2^* average. Their color corresponds to the color of the angle map. (Image taken from Hernández-Torres, . . . , Rauscher: PLOS ONE 2015.)

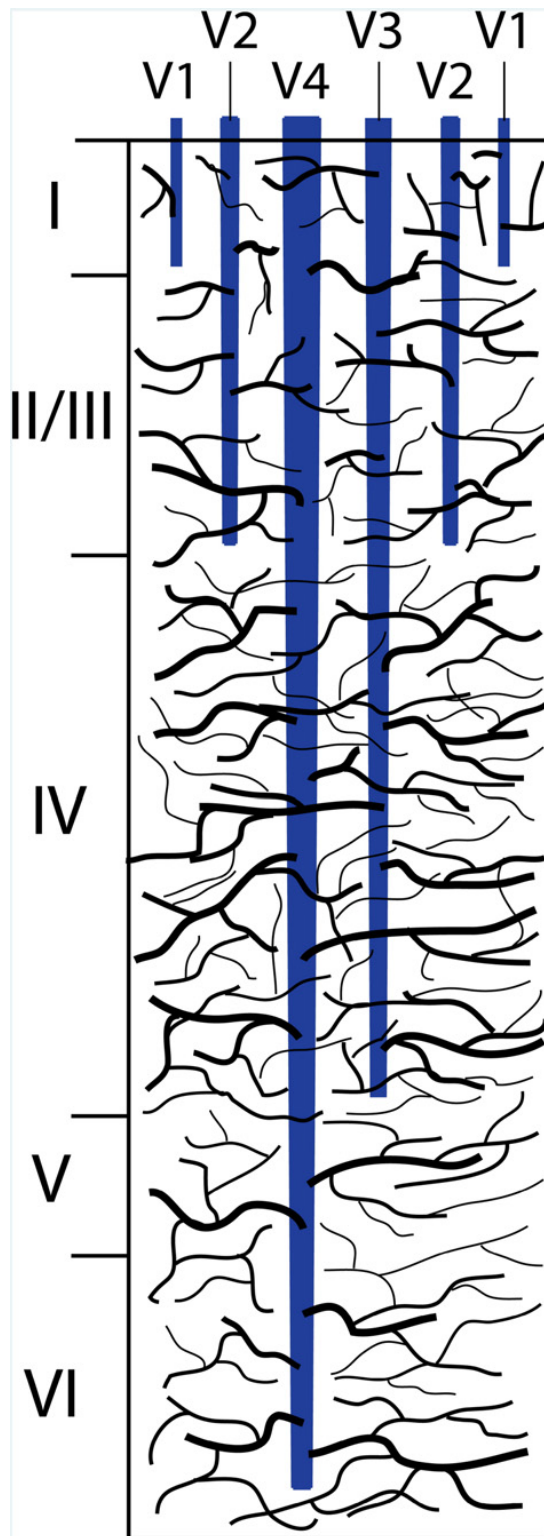


Figure S5, For Review Only: Figure 1 from Markuerkiaga, Barth & Norris, Neuroimage 2016 [72], showing different calibers of cortical veins at different cortical levels. See also Duvernoy, Delon, Vannson 1981 [68].